

# Characterising Strong Lensing Galaxy Clusters using the Millennium-XXL and MOKA simulations

Carlo Giocoli<sup>1\*</sup>, Mario Bonamigo<sup>1</sup>, Marceau Limousin<sup>1</sup>, Massimo Meneghetti<sup>2,3</sup>, Lauro Moscardini<sup>4,2,3</sup>, Raul E. Angulo<sup>5</sup>, Giulia Despali<sup>1,6</sup>, Eric Jullo<sup>1</sup>

<sup>1</sup> Aix Marseille Université, CNRS, LAM (Laboratoire d’Astrophysique de Marseille) UMR 7326, 13388 Marseille, France

<sup>2</sup> INAF - Osservatorio Astronomico di Bologna, via Ranzani 1, 40127 Bologna, Italy

<sup>3</sup> INFN - Sezione di Bologna, viale Berti Pichat 6/2, 40127 Bologna, Italy

<sup>4</sup> Dipartimento di Fisica e Astronomia, Alma Mater Studiorum Università di Bologna, viale Berti Pichat, 6/2, 40127 Bologna, Italy

<sup>5</sup> Centro de Estudios de Física del Cosmos de Aragón (CEFCA), Plaza San Juan 1, Planta-2, 44001 Teruel, Spain

<sup>6</sup> Max Planck Institute for Astrophysics, Karl-Schwarzschild-Strasse 1, 85740 Garching, Germany

July 16, 2018

## ABSTRACT

In this paper we investigate the strong lensing statistics in galaxy clusters. We extract dark matter haloes from the Millennium-XXL simulation, compute their Einstein radius distribution, and find a very good agreement with Monte Carlo predictions produced with the MOKA code. The distribution of the Einstein radii is well described by a log-normal distribution, with a considerable fraction of the largest systems boosted by different projection effects. We discuss the importance of substructures and triaxiality in shaping the size of the critical lines for cluster size haloes. We then model and interpret the different deviations, accounting for the presence of a Bright Central Galaxy (BCG) and two different stellar mass density profiles. We present scaling relations between weak lensing quantities and the size of the Einstein radii. Finally we discuss how sensible is the distribution of the Einstein radii on the cosmological parameters  $\Omega_M - \sigma_8$  finding that cosmologies with higher  $\Omega_M$  and  $\sigma_8$  possess a large sample of strong lensing clusters. The Einstein radius distribution may help distinguish Planck13 and WMAP7 cosmology at  $3\sigma$ .

**Key words:** Gravitational lensing: strong lensing – galaxy clusters; Numerical methods: simulations; Galaxies: clusters

## 1 INTRODUCTION

Spectroscopic galaxy redshift surveys and numerical  $N$ -body simulations have revealed a large-scale distribution of matter in the Universe featuring a complex network of interconnected filamentary galaxy associations (Tormen et al. 2004; Springel et al. 2005; The Dark Energy Survey Collaboration 2005; Sousbie et al. 2008, 2011; Guzzo et al. 2014; Percival et al. 2014; Le Fèvre et al. 2015; Codis et al. 2015). Vertices, i.e. interconnections among the filaments, correspond to the very dense compact nodes within this *cosmic web* where one can find massive galaxy clusters (Tormen 1998; Bryan & Norman 1998; Shaw et al. 2006; Borgani & Kravtsov 2011; Bellagamba et al. 2011).

The mass density distribution in clusters can be inferred using different wavelength observations (Meneghetti et al. 2010b; Donnarumma et al. 2011; Donahue et al. 2016). In

particular, optical and near-infrared data provided by, for instance, the Subaru and the Hubble Space telescopes (HST) are allowing to indirectly infer the total projected matter density distribution in clusters through its effect of gravitationally bending the light of background galaxies (Jullo et al. 2007; Merten et al. 2015; Limousin et al. 2015). Gravitational lensing, as predicted by the Einstein’s General Relativity, deflects light rays once they get close to a deep potential well (Einstein 1918; Landau & Lifshitz 1971). Light-rays from distant galaxies travelling in the space-time of our Universe can be weakly or strongly bent when they approach a galaxy cluster (Bartelmann & Schneider 2001; Bartelmann 2010). The weak lensing regime happens when the light-rays travel far from the centre of the cluster. In this case, the shapes of background galaxies are only slightly altered and, for a good determination of the signal, it is usually necessary to average over a large sample of background systems (Hoekstra et al. 2012, 2013; Giocoli et al. 2014; Radovich et al. 2015; Formicola et al. 2016). The strong lensing regime

\* E-mail: carlo.giocoli@lam.fr

takes place when the light-rays transit close to the centre of the cluster, and the mass density becomes critical: the lensing event in this case is non-linear and images of background galaxies may be multiplied and/or appear stretched and elongated. Depending on the quality of the data and on their availability, weak and strong lensing data can be used separately or jointly for a better reconstruction of the projected mass from the very central region to the outskirts of the cluster. In the following, we will concentrate on the strong lensing regime and on the objects that originate it, which we will refer to as Strong Lensing Clusters (SLCs).

SLCs may constitute a peculiar class of objects. While their existence is a natural consequence of General Relativity, “giant arcs” – extremely distorted images of background galaxies – hosted in clusters have been discovered only 30 years ago in the core of Abell 370, independently by Lynds & Petrosian (1986) and Soucail et al. (1987). This observation was recognised by Paczynski (1987) as the result of strong gravitational lensing, a hypothesis later confirmed by the measurement of the redshift of the arc (Soucail et al. 1988a,b).

Since then, SLCs have led to many important advances in cosmology: (*i*) being a direct and precise probe of the two-dimensional projected mass density, Strong Lensing (SL) has provided accurate mass maps, constraining structure formation properties and evolution scenarios (for example: Broadhurst et al. 2000; Sand et al. 2002; Saha & Williams 2006; Bradač et al. 2006; Zitrin et al. 2009a; Zitrin & Broadhurst 2009b; Newman et al. 2011; Verdugo et al. 2011; Sharon et al. 2014); (*ii*) producing a natural gravitational amplification, SL has allowed to push the frontier of our telescopes (for example: Richard et al. 2006; Coe et al. 2013; Atek et al. 2014; Zitrin et al. 2014); (*iii*) providing a method to probe the dark energy equation of state, since images position depends on the underlying cosmology (for example: Soucail et al. 2004; Jullo et al. 2010).

SLCs are now well established as a promising class of objects that cannot be ignored in cosmology, and their future is extremely promising, since future facilities are expected to detect thousands of SLCs (Laureijs et al. 2011; Boldrin et al. 2012, 2016; Serjeant 2014), and the exquisite resolution of the *James Webb Space Telescope* (JWST) will deliver unique multi-colour data sets for some of them. The growing importance of SLCs has been recently illustrated by the CLASH program (Postman et al. 2012) which has been awarded of 500 HST orbits to observe 25 massive SLCs. More recently, the Hubble Deep Fields Initiative has unanimously recommended a “Frontier Field” program of six deep fields concentrated on SL clusters (together with six deep “blank fields”) in order to advance our knowledge of the early epochs of galaxy formation and to eventually offer a glimpse of JWST’s universe (<http://www.stsci.edu/hst/campaigns/frontier-fields>). Each cluster will be imaged with 140 orbits, leading to a total of 840 orbits dedicated to the Frontier Field Initiative.

Very encouraging is also the work performed by Zitrin et al. (2011c) on reconstructing the mass density distribution and the Einstein radius (which estimates the size of the SL region) of a large sample of SDSS clusters. In this case, the “blind” approach based on the assumption that light traces mass has allowed to establish that the Einstein radius distribution of clusters with  $0.1 < z_l < 0.55$  has a log-normal

shape. Furthermore, a visual inspection has revealed that approximately 20 percent of SLCs are boosted by various projection effects.

Given the significance of SLCs, characterising this peculiar class of object is crucial and this has been the focus of many studies (for example: Hennawi et al. 2007; Meneghetti et al. 2010a; Redlich et al. 2012; Waizmann et al. 2012). This is also the motivation of the present work, where we aim at characterising which clusters do generate strong lensing features. Our approach is twofold: (*i*) first we will use the large sample of cluster statistics afforded by the Millennium-XXL simulation (Angulo et al. 2012) – exploiting its large size (3 Gpc/h box side), that allows to follow the formation of many massive haloes; (*ii*) second we will complement the statistics with a cosmological study based on clusters modelled using the MOKA code (Giocoli et al. 2012a).

We want to spend few words about the fact that the Einstein radius of lenses is not a direct observable quantity. The Einstein radius, defined by the location of the tangential critical lines (more will be discussed about this in the first section) is a byproduct of the mass reconstruction pipeline by mean of parametric algorithms that typically assume that mass traces the light (Jullo et al. 2007; Zitrin et al. 2011) or adaptively reconstruct the mass density distribution using non-parametric approaches (Merten 2014).

The paper is organised as follows: in Section 2 we present the numerical simulations and the pseudo-analytical methods we adopt as bases for our analyses; in Section 3 we discuss the scaling relations between the size of the Einstein radius and weak lensing-derived quantities; in Section 4 we present how the Einstein radius distribution depends on the matter content of the universe and on the initial normalisation of the power spectrum. Finally in Section 5 we summarise and discuss our results.

## 2 METHODS

In this paper we aim at studying the strong lensing properties of galaxy clusters – through the size of their Einstein radius – extracted from a very large cosmological box. However, the limitation of possessing the simulation only for one cosmological model in addition to the fact that the run has been performed only using collisionless dark matter particles forced us to complement the analyses using a pseudo-analytic approach to simulate convergence maps of triaxial clusters. This latter method allows us, in a more flexible way, to investigate which properties of clusters mainly contribute in shaping the Einstein radius, to quantify the contribution of the stellar component and to understand how the Einstein radius distribution of clusters may depend on specific cosmological parameters.

### 2.1 Strong lensing of Clusters in the Millennium-XXL Simulation

With a box side of 3 Gpc/h, the Millennium-XXL (M-XXL) simulation (Angulo et al. 2012) was especially tailored to study massive haloes which can be only found in very large volumes, because of their nature of extremely rare objects. The  $6720^3 \sim 3 \times 10^{11}$  dark matter particles have a mass of  $6.174 \times 10^9 M_\odot/h$ ; the Plummer-equivalent softening length

is  $\epsilon = 13.7$  kpc. For reasons of consistency with the previous Millennium runs (Springel et al. 2005; Boylan-Kolchin et al. 2009), the adopted  $\Lambda$ CDM cosmology as the following parameters total matter density  $\Omega_M = 0.25$ , baryons density  $\Omega_b = 0.045$ , cosmological constant  $\Omega_\Lambda = 0.75$ , power spectrum normalisation  $\sigma_8 = 0.9$  and dimensionless Hubble parameter in  $H_0/100$  km/s/Mpc  $h = 0.73$ . We remind the reader that the simulated volume of the M-XXL is equivalent to the whole observable Universe up to redshift  $z = 0.72$ .

At each simulation snapshot, haloes have been identified using a FoF algorithm. For each FoF-group, starting from the particle with the minimum potential, we then compute  $M_{200}$  as the mass enclosing a sphere 200 times denser than the critical density  $\rho_c$  at that redshift. In our analysis – for the motivation we will underline later – we will consider the halo catalogue at  $z = 1$  and the corresponding snapshot files. Due to the large number of haloes identified in the simulation volume we restrict our analysis only to the ones more massive than  $3 \times 10^{14} M_\odot/h$  – corresponding to 3135 systems. For each halo respecting this criterion we store all the particles enclosed in a cube of  $8 \text{ Mpc}/h$  by side and project them in a 2D-mass map resolved with  $2048 \times 2048$  pixels using the Triangular Shape Cloud technique, along six different directions. In the first three cases we consider three projections along the cartesian axes, which are then *random* with respect to the cluster morphology, we then consider three *peculiar projections* i.e. along the ellipsoid axes as computed in Bonamigo et al. (2015): major, intermediate and minor axes. In placing the particles on the grid, to avoid particle noise effects (Rau et al. 2013; Angulo et al. 2014) due to the discreteness of the dark matter density, we apply a Gaussian filter with a scale of  $3.25$  kpc/ $h$ , which corresponds to approximately one third of the simulation Plummer-equivalent softening.

From the constructed mass density maps  $\Sigma(x_1, x_2)$  – where  $x_1$  and  $x_2$  are the two cartesian coordinates on the 2D map projected in the plane of the sky – we compute the convergence  $\kappa(x_1, x_2)$  as:

$$\kappa(x_1, x_2) = \frac{\Sigma(x_1, x_2)}{\Sigma_{\text{crit}}} \quad (1)$$

with

$$\Sigma_{\text{crit}} \equiv \frac{c^2}{4\pi G} \frac{D_l}{D_s D_{ls}} \equiv \frac{c^2}{4\pi G} \frac{1}{D_{lens}} \quad (2)$$

where  $c$  represents the speed of light and  $G$  the universal gravitational constant;  $D_l$ ,  $D_s$  and  $D_{ls}$  are the angular diameter distances between observer-lens, observer-source and source-lens, respectively; we also define the lensing distance  $D_{lens} \equiv D_{ls} D_s / D_l$ . We assume clusters to be located at  $z_l = 0.5$  and sources at  $z_s = 2.5$ , computing the distances assuming the cosmological parameters in agreement with the Planck13 results (Planck Collaboration et al. 2014): the matter density parameter  $\Omega_M = 0.307$ , the contribution of  $\Lambda$   $\Omega_\Lambda = 0.693$ , the normalised Hubble constant  $h = 0.6777$  and the normalisation of the initial power spectrum  $\sigma_8 = 0.829$ . We do so because, even if the M-XXL simulation has been run with a different set of cosmological parameters, we assume to be able to rescale those clusters at  $z = 1$  from a M-XXL cosmology to a sample at  $z = 0.5$  in a Planck13 cosmology. This is supported by the fact that the halo properties at  $z = 1$  in the M-XXL cosmology are very similar to

those at  $z = 0.5$  in a Planck13 cosmology (Sheth & Tormen 1999; Macciò et al. 2008; Zhao et al. 2009; Giocoli et al. 2012b; Despali et al. 2015); even if the two mass functions for haloes more massive than  $3 \times 10^{14} M_\odot/h$  may be different by more than 50%, the two concentration-mass relations deviate by less than 5%.

From the convergence we can define the effective lensing potential as:

$$\Phi(x_1, x_2) \equiv \frac{1}{\pi} \int \kappa(\mathbf{x}') \ln |\mathbf{x} - \mathbf{x}'| d^2 \mathbf{x}', \quad (3)$$

with  $\mathbf{x} \equiv (x_1, x_2)$ , and then the pseudo-vector field of the shear  $\gamma = \gamma_1 + i\gamma_2$  as:

$$\gamma_1(x_1, x_2) = \frac{1}{2} (\Phi_{11} - \Phi_{22}), \quad (4)$$

$$\gamma_2(x_1, x_2) = \Phi_{12} = \Phi_{21} \quad (5)$$

with  $\Phi_{ij}$  representing the  $i$  and  $j$  derivatives of the effective lensing potential (Bartelmann & Schneider 2001; Bacon et al. 2010). At first order, gravitational lensing induces distortion and stretch on background sources: typically a circular source is mapped through gravitational lensing into an ellipse when both  $k$  and  $\gamma$  are different from zero. These effects are described by the Jacobian matrix:

$$A = \begin{pmatrix} 1 - \kappa - \gamma_1 & -\gamma_2 \\ -\gamma_2 & 1 - \kappa + \gamma_1 \end{pmatrix}. \quad (6)$$

The magnification is quantified as the inverse determinant of the Jacobian matrix that can be read as:

$$\mu \equiv \frac{1}{\det A} = \frac{1}{(1 - \kappa)^2 - \gamma^2}; \quad (7)$$

the inverse of the eigenvalues of the Jacobian matrix measure the amplification in radial and tangential direction of background sources:

$$\mu_r = \frac{1}{1 - \kappa + \gamma} \quad (8)$$

$$\mu_t = \frac{1}{1 - \kappa - \gamma}. \quad (9)$$

For circularly symmetric lenses, the regions in the image plane where the denominator of the relations above is equal to zero define where the source images are infinitely radially and tangentially magnified, respectively. In particular images forming close to the tangential critical curve are strongly distorted tangentially to it.

The definition of critical curves is more complex and non trivial in asymmetric, substructured and triaxial clusters. From each convergence map the lensing potential and the shear are numerically computed in Fourier space<sup>1</sup> where derivatives are easily and efficiently calculated. To avoid artificial boundary effects each map is enclosed in a zero-padded region of 1024 pixels. We have tested the impact of the size of the zero-padded regions on the weak and strong lensing properties of individual non-periodic cluster maps and find that artefact mirror clusters do not appear when the size of the zero region is at least half of the considered field of view. To define the Einstein radius of the cluster we identify in the cluster maps points of infinite tangential

<sup>1</sup> using the FFTW libraries: <http://www.fftw.org>

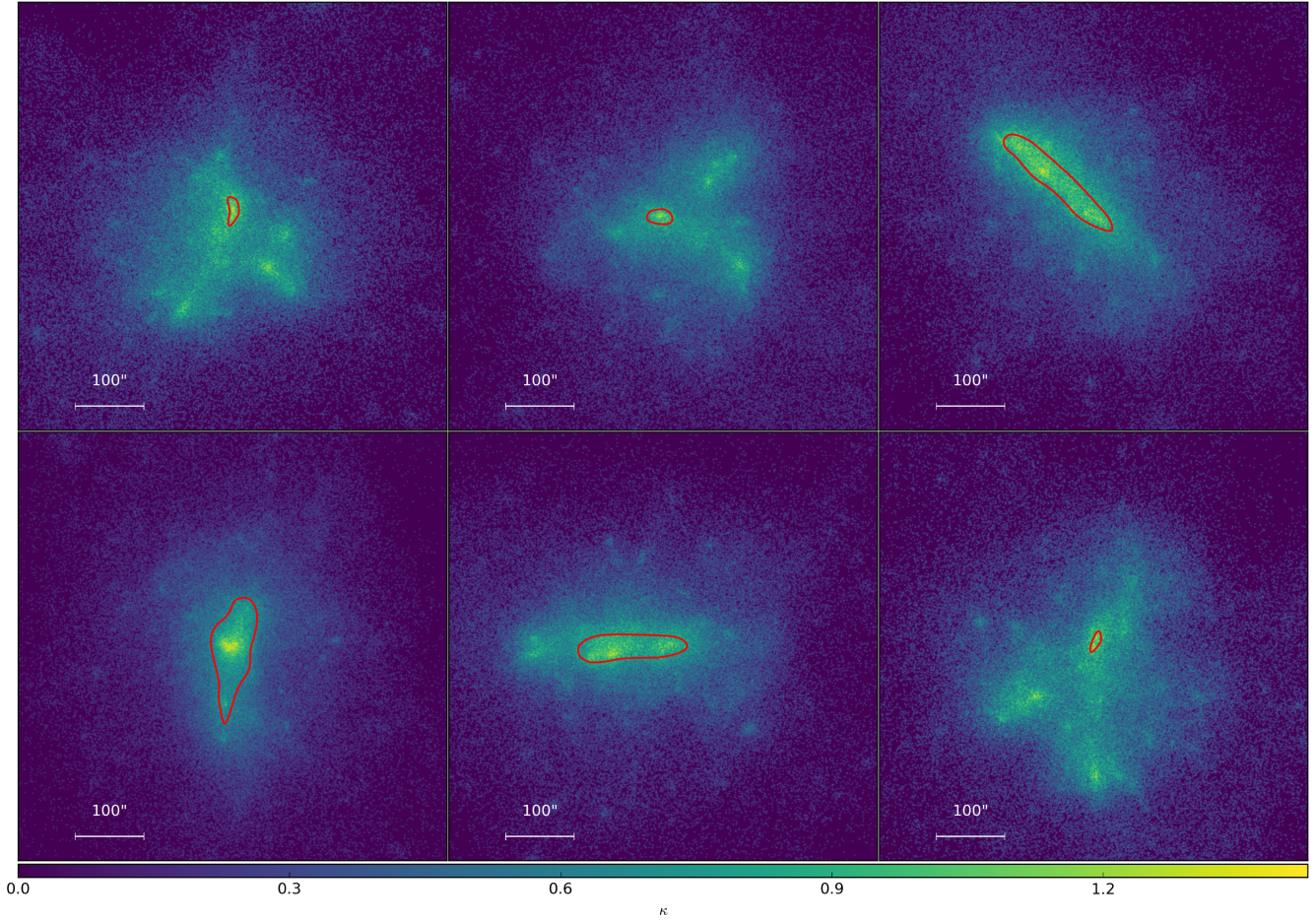


**Figure 1.** Convergence maps of different projections of a halo extracted from the Millennium-XXL simulation with mass  $M_{200} = 1.2 \times 10^{15} M_{\odot}/h$ . The red curves in each panel represent the tangential critical lines from which we compute the median Einstein radii. The top-three images show the three projections along the cartesian axes (i.e. *random* with respect to the cluster morphology), while the bottom ones from left to right, are the projections along the major, intermediate and minor axes, respectively. This particular cluster has the peculiarity of having in one projection (namely the one in the left bottom panel) the largest Einstein radius in our sample: 75 arcsec.

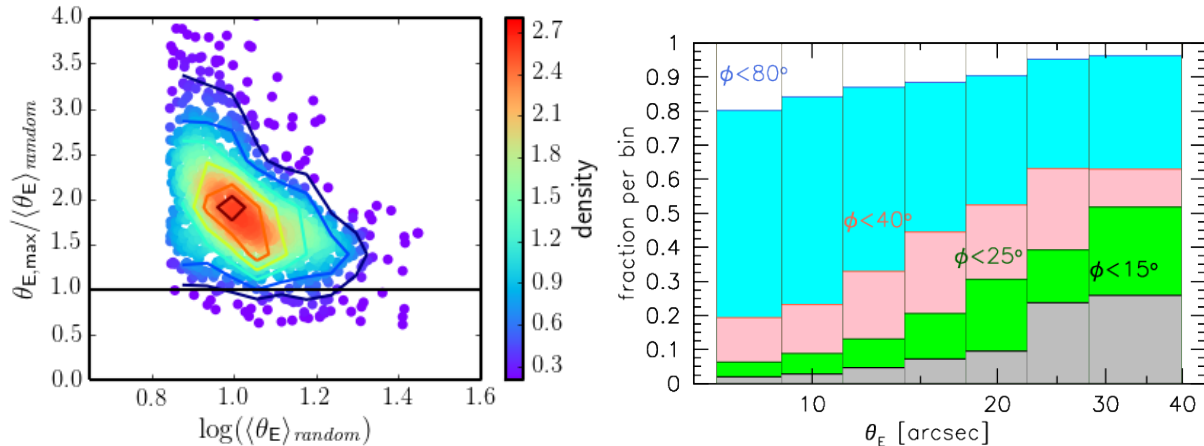


**Figure 2.** Left panel: scatter plots of the relative size of the Einstein radii when the cluster major axis of the ellipsoid is oriented along the line-of-sight with compared to the average value of the three *random* projections:  $\langle \theta_E \rangle_{random}$ . Right panel: Fraction  $i$  of clusters with an angle  $\phi$  between the direction of the major axis of the mass ellipsoid and the line-of-sight smaller than  $80^\circ$ ,  $40^\circ$ ,  $25^\circ$  and  $10^\circ$  as a function of the Einstein radius.

**Table 1.** Percentage of the projections along which M-XXL clusters have the largest Einstein radius for the *random* and the *peculiar* projections, respectively.

projection	% ( <i>random</i> )
<i>x</i>	34%
<i>y</i>	32%
<i>z</i>	34%
projection	% ( <i>peculiar</i> )
major axis of the ellipsoid	86%
intermediate	12%
minor	2%

magnification  $\theta_t$  and define the Einstein radius  $\theta_E$  as the median distance of these points from the cluster centre:

$$\theta_E \equiv \text{med} \left\{ \sqrt{(\theta_{i,x_1} - \theta_{c,x_1})^2 + (\theta_{i,x_2} - \theta_{c,x_2})^2} \mid \theta_i \in \theta_t \right\}. \quad (10)$$

We define the center of the cluster  $\theta_c$  as the position of the particle with minimum potential and the connected region defined by the tangential critical points  $\theta_t$ , when they exist, have to enclose the cluster centre; this ensures that the critical points are not eventually assigned to a substructure present in the field of view. The robustness of this definition has already been tested and discussed in a series of works (Meneghetti et al. 2008, 2010a; Redlich et al. 2012; Giocoli et al. 2014) to which we remind the reader for more details. The size of the Einstein radius defines a measure of the strong lensing region and, for an axially symmetric lens, permits to estimate the mass enclosed within it using the equation:

$$\theta_E = \left( \frac{4GM(< \theta_E)}{c^2} \frac{D_{ls}}{D_l D_s} \right)^{1/2} \quad (11)$$

assuming that all mass is located at the centre of the lens. By geometrically measuring the area  $A$  enclosed by the tangential critical curve it is possible to define the effective Einstein radius as  $\theta_{E,eff} = \sqrt{A/\pi}$ . However, we will rely on the median Einstein radius definition that – as noticed by Meneghetti et al. (2011) and Giocoli et al. (2014) – better captures the presence of asymmetries of the matter distribution towards the cluster centre.

In Figure 1 we show the six considered projections of the halo which in one them has the largest Einstein radius (75 arcsec) in our constructed catalogue – namely in the bottom left panel. The top panels show the *x*, *y* and *z* projections, while the bottom ones the projections along the major, intermediate and minor axis of the halo ellipsoid, from left to right respectively. In each panel, the red curves represent the tangential critical curves, i.e. where images of background galaxies would appear highly tangentially magnified if located close to the optical axis of the lens system. From the figure we notice that the largest Einstein radius occurs, in this case – as in most of the cases, when the major axis of the cluster ellipsoid is oriented along the line-of-sight; the opposite holds when the minor axis points towards the observer. From the measured Einstein radius of each of the six projections of all clusters in the M-XXL we can summarise (as it can be read in Table 1) that in the *random projections* the probability of having the largest Einstein radius is

uniform in the three cases as expected. However, considering the *peculiar projections*, sample we notice that in 86% of the cases the largest Einstein radius appears when the major axis of the ellipsoid is oriented along the line-of-sight and in 12% (2%) of the cases when the orientation is the intermediate (minor) axis. We have investigated those latter cases and they arise either (i) when there is a merging event which manifests in the presence of a massive substructure projected in correspondence of the cluster centre and/or (ii) when the cluster ellipsoid is very elongated in the plane of the sky.

In the left panel of Figure 2 we quantify by how much the Einstein radius grows when the cluster is oriented along the major axis of its mass ellipsoid. We consider all clusters having at least an Einstein radius of 7 arcsec along one of the considered projections<sup>2</sup>. In this case we compare the size of the Einstein radius computed when the cluster is oriented along the major axis with respect to the average value measured from its three *random projections*. From the figure we observe that the typical size of an Einstein radius may grow up to a factor of two/three when the cluster is aligned along the line of sight with respect to a random orientation; we also notice some cases where the Einstein radius computed in a *random projection* is larger than the value measured when the mass ellipsoid is oriented along the line-of-sight; as discussed previously we verified that those cases are merging clusters or very elongated ellipsoids in the plane of the sky. All this brings more light to the general picture that most of the strong lensing clusters may possess their dark matter halo major axis preferentially pointing close to the line-of-sight (Oguri & Blandford 2009). This is more evident in the right panel of the same figure where we show the fraction of SLCs per different bins in  $\theta_E$  that possess an angle  $\phi$  between the major axis of the ellipsoid and the line-of-sight smaller than a given value: 65% of SLCs with  $30 < \theta_E < 40$  have an angle  $\phi$  between the direction of their major axis and the line-of-sight smaller than 40 degrees. Our finding are quite consistent with the results presented by Oguri et al. (2005) where the authors also discuss that the apparent steep observed mass profile can be reconciled with theoretical models if the triaxial ellipsoid of the dark matter halo is preferentially oriented with the major axis along the line-of-sight.

However, when looking at random projections in the plane of the sky, the sole effect of triaxiality is less obvious. Figure 3 shows the difference that might arise in the distribution of shapes – namely minor to major axis ratio  $s$  – by selecting clusters that are strong lenses (blue histograms) instead of the general population (black histograms). Haloes have been subdivided in bins of Einstein radius  $\theta_E$ , each shown in a different panel. Even though, as previously found by Hennawi et al. (2007), the distribution of the axis ratio of SLCs does not seem to differ from the distribution of the overall population, the mean values (vertical dashed lines) vary up to 5%, in particular for very large  $\theta_E$ . A Kolmogorov-Smirnov test showed that we can reject the hypothesis that the samples are taken from the same distri-

<sup>2</sup> The value of 7 arcsec ensures that the measurement of the size of the Einstein radius of the cluster is not affected nor by particle noise neither by the finite grid size of the map.

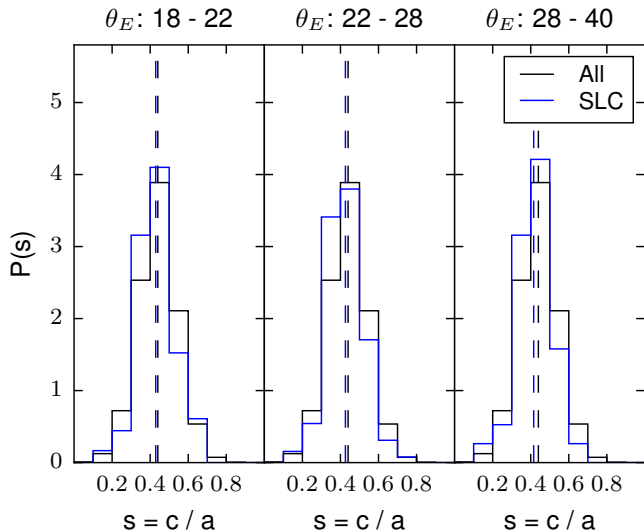


**Figure 3.** Probability distribution functions of the minor to major axis ratio of the overall M-XXL cluster population (black histogram) and of the SLCs (blue histogram), with each panel representing a different bin in  $\theta_E$ . Vertical dashed lines indicate the mean of the corresponding sample.

bution at significance level of 10%, meaning that there is a low probability that SLC have the same shape properties of the overall population. This suggests that the concentration is mainly responsible in driving the correlation of the cluster Einstein radii.

It is important to underline that the effect of correlated and uncorrelated large scale structures may also impact the lensing properties of galaxy clusters and boost their strong lensing cross section as well as the size of the Einstein radius (Puchwein & Hilbert 2009). Usually to quantify the impact of uncorrelated structures along the line-of-sight it is necessary to run expensive multi-plane ray-tracing lensing simulations of clusters and matter extracted from cosmological runs (Hilbert et al. 2008; Petkova et al. 2014; Giocoli et al. 2015), things that are beyond the purpose of this paper. However the effect of correlated structures on the lensing properties can be studied selecting for each cluster projection a larger region along the line-of-sight, and quantify how these changes on the determination of the Einstein radius. To do so, we have produced two other sets of convergence maps, one selecting particles from a region of 16 Mpc/h and another from 32 Mpc/h along the line-of-sight, and projecting all of them into a single lens plane. We still keep the size of the region in the plane of the sky to be 8 Mpc/h of a side. As an example, in Figure 4 we show the average convergence power spectra of the *random projections* sample considering a region of 8, 16 and 32 Mpc/h along the line-of-sight in black, blue and red, respectively. In the bottom panel we present the relative residuals of the last two cases with respect to the 8 Mpc/h reference one. We notice that the inclusion of more matter along the line-of-sight tends to increase the convergence power spectrum at small scales of about 20 percent for 16 Mpc/h and almost 40 percent for 32 Mpc/h, which however contains 4 times the volume. In the figure we show also for comparison the prediction from a smooth NFW halo (green curve) and the power spectrum of a spherical halo (with the same large

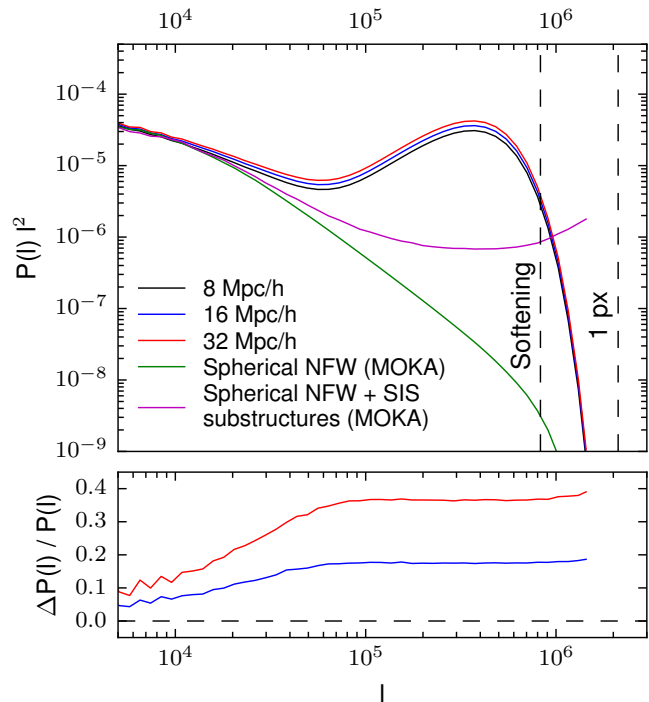


**Figure 4.** Average convergence power spectrum of haloes of the M-XXL simulation. Black, blue and red curve show the average power spectrum derived extracting the particles contained in a region of 8, 16 and 32 Mpc/h along the line-of-sight; in the plane of the sky in all three cases we have considered particles in a square of 8 Mpc/h of side. The green curve shows the prediction from smooth NFW spherical haloes, while the purple one presents the prediction for spherical MOKA haloes with substructures modelled with a Singular Isothermal Sphere (SIS) profile. The bottom panel shows the relative residuals of the average power spectra measured using 16 and 32 Mpc/h with respect to the one computed assuming 8 Mpc/h as box side along the line-of-sight.

scale normalisation) with substructures (in magenta): both curves are obtained by averaging produced using MOKA haloes (see below), with the same masses and NFW concentrations of the M-XXL sample. In this case we observe that the presence of substructures in a halo tends to increase the small scale power of more than one order of magnitude for  $l \gtrsim 3 \times 10^4$  with respect to a smooth case. The other interesting behaviour is that while the power spectrum of haloes extracted from the M-XXL are characterised at small scales by the particle noise and finite grid size of the maps (Vale & White 2003), MOKA haloes are particle noise-free and the only numerical limitation at small scale is set by the desired grid size of the map.

Puchwein & Hilbert (2009) have shown that the presence of uncorrelated structures tends to boost both the strong lensing cross-section for giant arcs and the size of the Einstein radii. As discussed, an accurate description of the contribution of uncorrelated large-scale structures needs expensive multi-plane ray-tracing simulations and is beyond the purpose of this paper. However in order to give a hint on how much the Einstein radii change including more matter along the line-of-sight, in Figure 5 we show the relative size of the Einstein radius – with respect to the case in which we select a region of 8 Mpc/h along the line-of-sight – computed selecting a region of 16 Mpc/h (left) and 32 Mpc/h

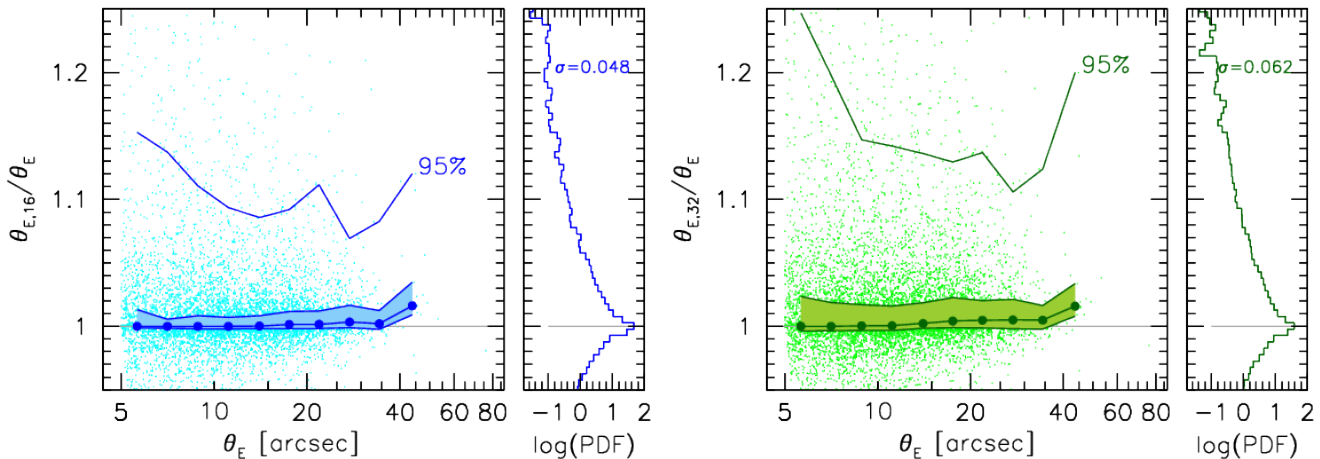


**Figure 5.** Relative change of the Einstein radius of strong lensing clusters extracted from the M-XXL simulation when we include all the matter from a region up to 16 Mpc/h (left) and 32 Mpc/h along the line-of-sight. As a reference we consider the Einstein radii as computed from the run where we select all the matter up to 8 Mpc/h. The filled circle points show the median of the distribution, while the shaded area encloses the first and the third quartiles of the distribution at fixed  $\theta_E$ .

(right) along the line-of-sight. From the figure we can observe that the median value is consistent with unity (filled blue points) and that, in some cases, large scale structures may boost the size of the Einstein radius even by 30%. We notice also that this population is less than 5% of the whole sample. The shaded regions in the figure enclose the first and the third quartiles of the distribution at fixed  $\theta_E$ . In each panel, the solid line encloses 95% of the data. The histogram in the right sub-panels shows the distribution along the y-axis together with the value of the standard deviation of the distributions.

## 2.2 Strong lensing models of Clusters using the MOKA code

Running and analysing large numerical simulations are usually non trivial tasks; in addition performing self consistent lensing analysis of different cosmological models including also baryon physics requires large computational resources and various post-processing pipelines. However, the results from different numerical simulations –  $N$ -body only or including hydrodynamical processes – can be implemented using a pseudo-analytic approach to construct convergence maps of different galaxy clusters in various physical cases as, done with the MOKA code (Giocoli et al. 2012a). MOKA pseudo-analytically reconstructs high-resolution convergence maps of galaxy clusters free from particles and numerical resolution limitations, implementing results obtained from the most recent numerical runs. The virial mass of a halo is defined as

$$M_{vir} = \frac{4\pi}{3} R_{vir}^3 \frac{\Delta_{vir}}{\Omega_m(z)} \Omega_0 \rho_c, \quad (12)$$

where  $\rho_c$  represents the critical density of the Universe,  $\Omega_0 = \Omega_m(0)$  the matter density parameter at the present time and  $\Delta_{vir}$  is the virial overdensity (Eke et al. 1996; Bryan & Norman 1998),  $R_{vir}$  symbolises the virial radius of the halo which defines the distance from the halo centre that encloses the desired density contrast. Haloes typically follow the NFW profile and are assumed to be triaxial – following

the model by Jing & Suto (2002) and randomly oriented with respect to the line-of-sight. Each system is also populated by dark matter substructures assuming the subhalo population model by Giocoli et al. (2010a). In modelling the subhalo density profiles we account for tidal stripping due to close interactions with the main halo smooth component and to close encounters with other clumps, gravitational heating, and dynamical friction (Hayashi et al. 2003; van den Bosch et al. 2005; Choi et al. 2007; Giocoli et al. 2008) using a truncated singular isothermal sphere (Metcalf & Madau 2001). For the halo concentration-mass relation we use the Zhao et al. (2009) model which links the concentration of a given halo with the time ( $t_{0.04}$ ) at which its main progenitor assembles 4 percent of its mass – each halo mass accretion history is computed using the results by Giocoli et al. (2012b). Haloes may also be populated by galaxies according to a HOD approach (Wang et al. 2006) and once settled the central galaxy, with a given stellar mass profile, the surrounding dark matter distribution can adiabatically contract (Blumenthal et al. 1986; Keeton 2001; Gnedin et al. 2011). To model the stellar mass density profile MOKA has two implementations: the the Hernquist (Hernquist 1990) and Jaffe (Jaffe 1983) profiles. Both for the Hernquist and the Jaffe profiles we compute the central galaxy scale radius  $r_g$  from the the half-mass (or effective) radius  $R_e$  by  $r_g = 0.551R_e$  and as done by Keeton (2001) we define the effective radius to be  $R_e = 0.003R_{vir}$ . The contribution of all the components are then summed together to compute the cluster convergence map as it can be read from the relation:

$$\begin{aligned} \kappa(x, y) = & \kappa_{DM}(x, y) + \\ & \kappa_{star}(x, y) + \sum_{i=1}^N \kappa_{sub,i}(x - x_{c,i}, y - y_{c,i}), \end{aligned} \quad (13)$$

where  $x_{c,i}$  and  $y_{c,i}$  represent the coordinates of the center of mass of the  $i$ -th substructure. The code is very fast and allows not only to study the dependence of lensing observables on the halo properties but also to perform different cosmological studies (Boldrin et al. 2012, 2016) and comparisons with various observational data (Xu et al. 2015), presenting

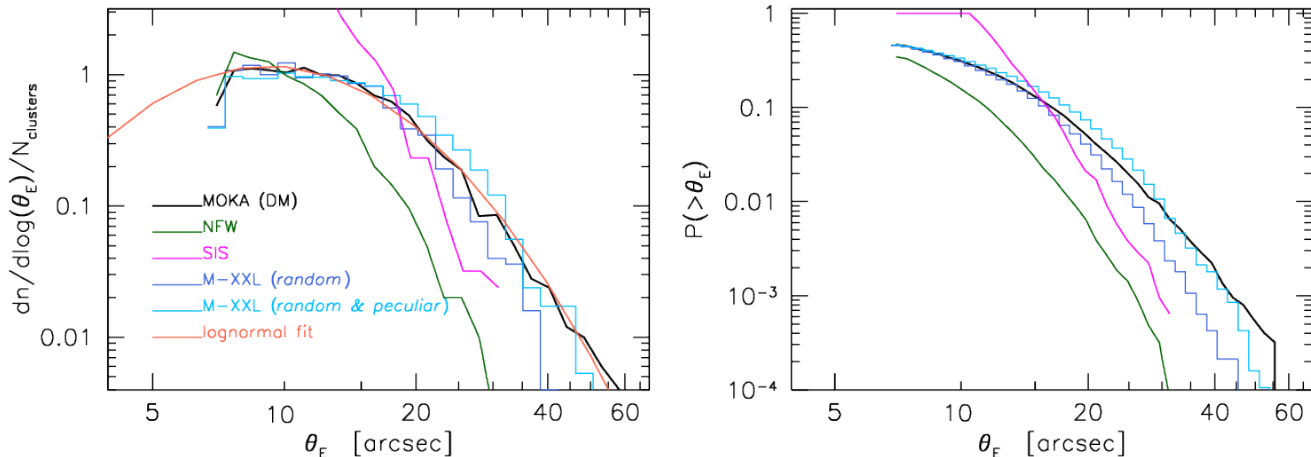


**Figure 6.** Differential (left panel) and cumulative (right panel) Einstein radius distributions in M-XXL and MOKA clusters. The blue and cyan histograms show the distributions measured in the M-XXL simulation considering only the *random projections* and all the six ones, respectively. The black curve represents the predictions obtained with a MOKA DM run on the same cluster masses, while the green and magenta ones are the predictions for the same masses assuming a smooth NFW or SIS halo profile for the lenses.

**Table 2.** Summary of MOKA runs performed with different models for the central galaxy.

run	triaxiality	minimum $m_{sb}$	BCG profile	DM Adiabatic Contraction
sDM	NO	$10^{10} M_{\odot}/h$ & $10^{12} M_{\odot}/h$	NO	NO
DM	YES	$10^{10} M_{\odot}/h$	NO	NO
H	YES	$10^{10} M_{\odot}/h$	Hernquist	YES
J	YES	$10^{10} M_{\odot}/h$	Jaffe	YES

great complementarity also with approaches used in various observational studies (Jullo et al. 2007; More et al. 2012).

In Figure 6 we compare the Einstein radius distributions of different MOKA cluster realisations of the mass sample extracted from the M-XXL catalogue at  $z = 1$  having  $M_{200} > 3 \times 10^{14} M_{\odot}/h$  and  $\theta_E > 7$  arcsec. We remind the reader that for this comparison we did not generate haloes from the corresponding theoretical mass function but we provide MOKA a sample of clusters with the same masses as the ones in the M-XXL simulation extracted at  $z = 1$ . Lenses are then located at  $z_l = 0.5$  and sources at  $z_s = 2.5$ . On the left we show the differential distributions normalised to the total number of clusters while on the right the cumulative ones. To be consistent with the numerical simulation, MOKA haloes have been generated without a Bright Central Galaxy (BCG) and have a c-M relation as for the M-XXL cosmology at  $z = 1$ , computed using the Zhao et al. (2009) model adopting the Giocoli et al. (2012b) halo mass accretion history model. The blue and the cyan histograms show the measurements from the M-XXL considering only the three *random projections* and considering all the six ones – *random* plus *peculiar projections*, respectively. The MOKA maps have been created with a resolution of  $1024 \times 1024$  pixels and are extended up the virial radius scale of the cluster. As in the M-XXL analysis we compute the lensing potential and the shear going in the Fourier space and to avoid artificial boundary effects we enclose the maps in a zero-padded region of 512 pixels. The black solid line shows the predictions for different MOKA realisations of the same cluster mass sample. For comparison the green and the magenta curves show the Einstein radius distributions computed as-

suming a smooth spherical NFW (Navarro et al. 1996) and Singular Isothermal Sphere (SIS) halo sample. The latter profile is typically used to predict the location of strong lensing images in elliptical galaxies (Koopmans et al. 2006, 2009). We estimate the velocity dispersion of the SIS halo we adopt the definition depending on the halo virial mass and radius according to the spherical collapse model (Wu et al. 1998; Cooray & Sheth 2002). The figure suggests a quite good consistence in the Einstein radius statistics between MOKA and M-XXL clusters, and also that a simple spherical NFW model highly under-predicts the strong lensing capability of SLCs with respect to a triaxial and substructured case. As done by Zitrin et al. (2011c), we describe our results with a log-normal distribution (red curve in the left panel of the figure): the relation has  $\mu = 2.219$  and  $\sigma = 0.532$  normalised consistently as done for the computed distribution from our data; approximately 47% of the clusters with  $M_{200} > 3 \times 10^{14} M_{\odot}/h$  possess an Einstein radius larger than 7 arcsec.

In Figure 7 and 8 we discuss the effect of triaxiality and substructures on the size of the Einstein radius. Going step-by-step, in the first figure we compare the size of the Einstein radii of the same sample of haloes when running MOKA with the triaxiality off (spherical sDM) and on (triaxial DM), keeping identical all the other cluster and map properties. The effect of triaxiality, as already discussed by different authors studying haloes in numerical simulations (Jing & Suto 2002; Despali et al. 2014), is quite crucial and typically tends to boost the Einstein radius even by a factor of four. Nevertheless, it is important to observe that the scatter around unity is quite asymmetric and depends on



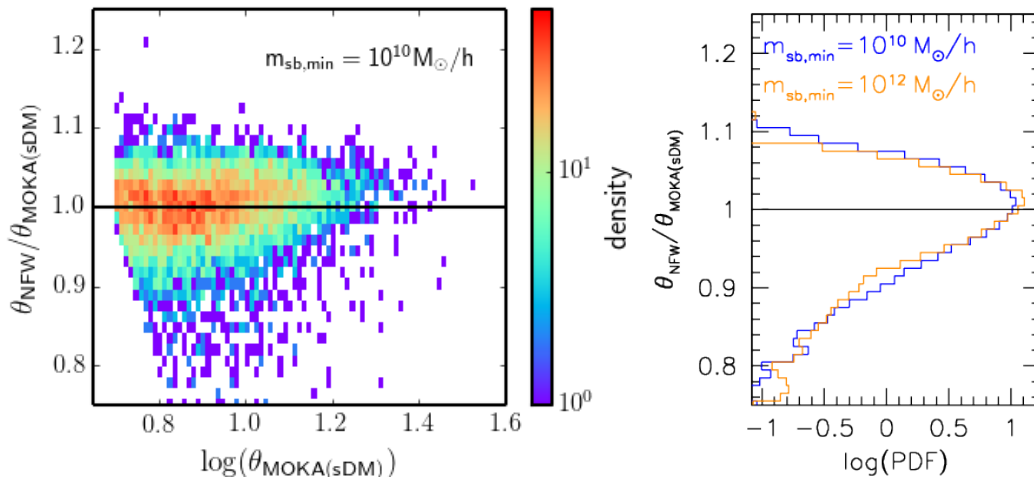


**Figure 8.** Effect of substructures in perturbing the Einstein radius of galaxy clusters. Relative variation of the size of the Einstein radius in presence of substructures. To isolate the effect we consider the case of spherical clusters. In the left panel we show the density probability distribution of the relative variation assuming  $10^{10} M_{\odot}/h$  as minimum subhalo mass. In the right panel we present the Probability Distribution Function distributions of the Einstein radius variation for the two subhalo minimum mass cases:  $10^{10}$  and  $10^{12} M_{\odot}/h$ .

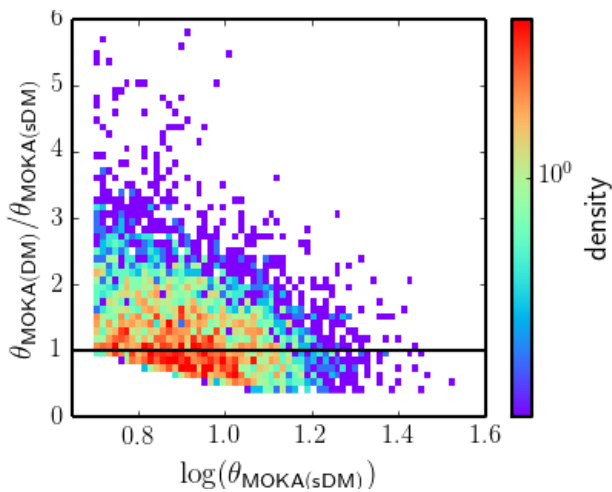


**Figure 7.** Effect of triaxiality in distorting the size of the Einstein radius. Relative size of the Einstein radius between a smooth spherical and triaxial NFW halo as obtained from MOKA.

how the halo ellipsoid – typically prolate – is oriented with respect to the line-of-sight. On the other side, in Figure 8 we isolate the effect of substructures performing two sets of simulations for our halo sample. In the first we consider a spherical DM halo populated with substructures down to  $m_{\text{sb}} = 10^{10} M_{\odot}/h$  and in the second down to  $10^{12} M_{\odot}/h$  for the minimum subhalo mass and compare their results with respect to a smooth and spherical NFW sample. In the left panel of the figure we compare the size of Einstein radii of clusters in our first run with respect to the size computed from a smooth NFW halo with the same mass and concentration. We remind the reader that in populating a halo with substructures we use the model by Giocoli et al. (2010a) for the subhalo mass function and the results by Gao et al. (2004) for the subhalo distribution in the host. Once the subhalo mass function is sampled we compute the total mass in subhaloes and subtract it to the input halo mass to compute

the smooth halo component, to which we assign a concentration such that the mass density profile of the smooth plus clump components matches the input assigned concentration. In the right panel of Figure 8 we show the probability distribution function of the relative Einstein radius variation between the smooth NFW halo and the substructured runs with the two different minimum subhalo mass thresholds. We notice that the presence of small substructures tends to perturb the size of the Einstein radius, but are the most massive ones that mainly contribute to distort the strong lensing regions – although this depends on the relative distance of the perturber from the critical curves of the cluster.

A correct treatment of the mass density distribution in the central region of the cluster is very important for strong lensing modelings and predictions (Meneghetti et al. 2003). Numerical simulations and semi-analytical models forecast that merger events (Springel et al. 2001b; De Lucia et al. 2004; Tormen et al. 2004) that drive the formation of dark matter haloes along the cosmic time bring to the formation of a massive and bright galaxy at the centre of galaxy clusters (Merritt 1985). These central galaxies are typically the brightest galaxies in clusters and are usually referred as Brightest Central Galaxy (BCG). They are the most massive galaxies in the Universe and generally are giant ellipticals: their position correspond approximately to the geometric and kinematic centre of the cluster and to the position of the peak of the X-ray emission. Nevertheless, it is interesting to mention that there are clusters where these conditions are not all satisfied at the same time: typically this happens in systems that are not completely relaxed and present merging events (Katayama et al. 2003; Sanderson et al. 2009; Zhang et al. 2016). For the density distribution of the stars in the BCG, in our analyses we make use of two different parameterisations: the Hernquist (Hernquist 1990) and the Jaffe (Jaffe 1983) profiles. We remind the reader that in running MOKA with these parameterisations we (i) assign the stellar mass to the BCG using a HOD formalism (Wang et al. 2006), (ii) conserve the total mass in the cluster and

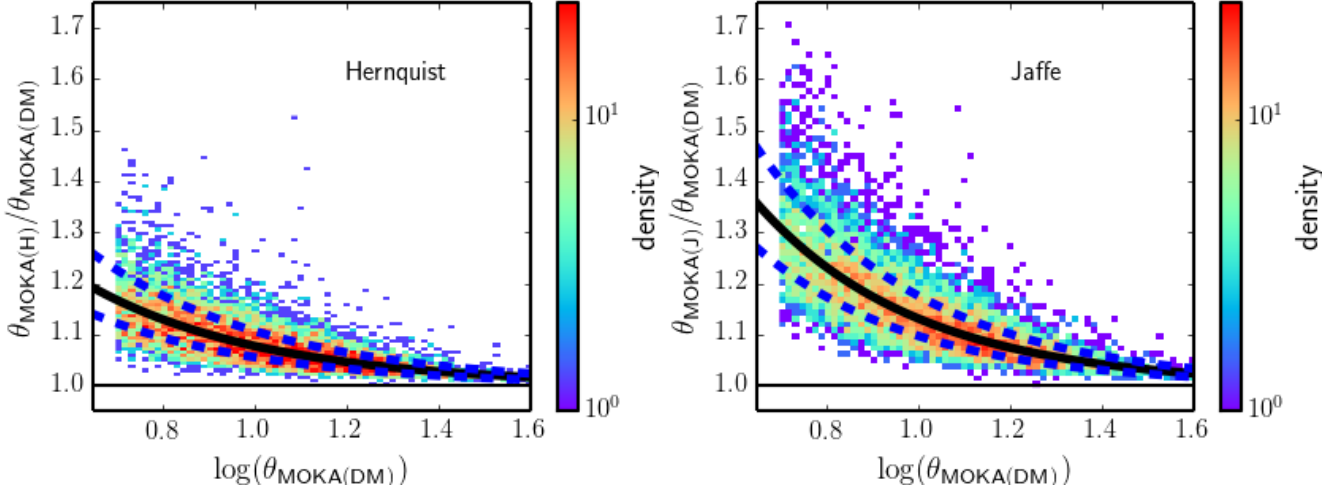


**Figure 9.** Influence of the presence of a Bright Central Galaxy (BCG) in modifying the size of the Einstein radius. Left and right panels refer to the case of a BCG with a Hernquist and Jaffe profile, respectively. The solid curve in each panel represents the best fit relation to the scatter distribution as it can be read from eq. (14). The dashed curve shows  $1\sigma$  uncertainties on the measured best fit parameters.

(iii) allow the dark matter density distribution to adiabatically contract (Keeton 2003; Giocoli et al. 2012a). In Figure 9 we show the relative size of the Einstein radius for strong lensing clusters (with  $\theta_E > 5$  arcsec – below which our measurements may be affected by the grid size of the map) between a pure DM run and a set of simulations that assume a Hernquist (left panel) and a Jaffe profile (right panel) for the BCG. Because of the different behaviour of the profile, the two models give quite different relative results. We remind the reader that while the Hernquist profile has a logarithmic slope in the inner part of  $-1$ , the Jaffe profile goes like  $-2$  and both profiles in the outskirts of the BCG proceed like  $-4$ . From the figure we notice that for smaller values of Einstein radii the results are dominated by the mass density distribution of the BCG, on the contrary for larger values of  $\theta_E$  they are influenced by the dark matter profile: triaxiality plus clumpiness of the halo. In the figures the solid curves represent the best fit relation to the scattered data points; they can be, respectively, read as:

$$\theta_E/\theta_{E,(DM)} = A \exp(\beta\theta_{E,(DM)}) \quad (14)$$

Hernquist	$A = 0.024_{-0.281}^{+0.251}$	$\beta = -2.579_{-0.051}^{+0.070}$
Jaffe	$A = 0.817_{-0.242}^{+0.217}$	$\beta = -2.843_{-0.059}^{+0.075}$

the dashed curves show the  $1\sigma$  uncertainties on the relations.

The benefit of having these fitting functions is illustrated in Figure 10, where we compare the cumulative probability distribution computed from a pure DM run (black curve) and from the two runs that assume the Hernquist (orange curve) and Jaffe (purple curve) profiles for the central galaxy. In the bottom panel, we present the relative residuals of the cumulative distributions of the two runs with BCG with respect to the DM-only case. The presence of a BCG increases the probability of having a cluster with an Einstein radius larger than  $\theta_E > 10$  arcsec of about 10 – 20% – depending on the density profile model of the central galaxy. In the bottom panel the two corresponding dashed coloured curves show the relative distributions obtained from the pure DM results and accounting for the BCG contribution sam-

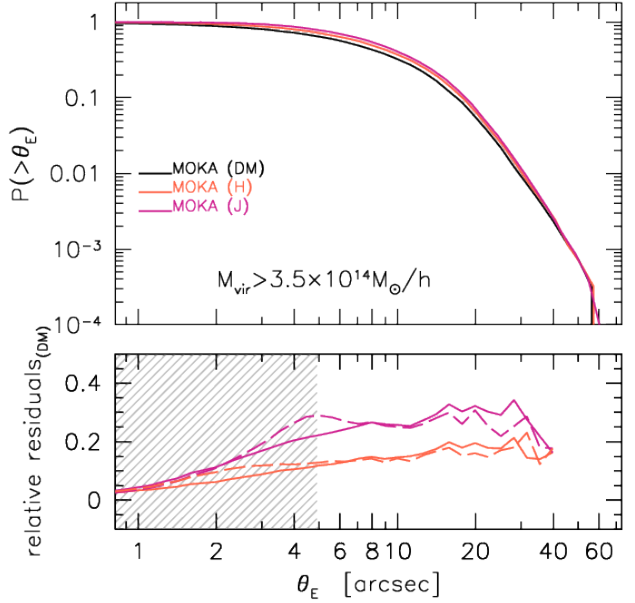


**Figure 10.** Cumulative probability distribution of having a cluster with an Einstein radius larger than a given value. Black, orange and salmon coloured curves show the distribution computed from a MOKA Monte Carlo Simulation of the M-XXL mass sample assuming no BCG (DM) a BCG with a Hernquist (H) or a Jaffe (J) profile, respectively. The solid curves in the bottom panel show the relative residuals of the distributions with respect to the DM only case. The dashed curves refer to the predictions of the Einstein radius distributions computed for the two cases from the DM run using the relation as in eq. 14.

pling the best fitting relations as in eq. 14 with their appropriate scatter for the parameters.

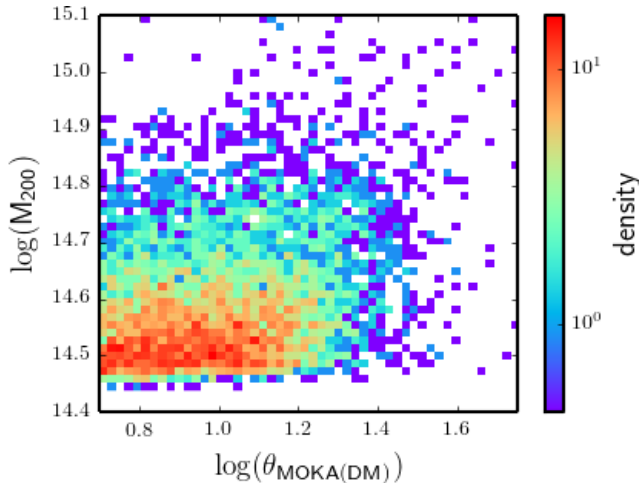


**Figure 11.** Correlation between the cluster masses and the measured size of the Einstein radii from the two-dimensional convergence maps. The colours show the point density of clusters of the DM-only MOKA run in the  $\log(M_{200})$ - $\log(\theta_E)$  space.

### 3 STRONG LENSING SCALING RELATIONS

In this section we discuss the correlation of the size of the Einstein radius with other galaxy cluster properties. In the figures we will present we have used the only-DM MOKA runs; the relations obtained considering runs with a BCG following a Hernquist and a Jaffe profile will be summarised in Table 3.

The first correlation we have considered is between the cluster mass and the size of the Einstein radius (see Fig 11). In this case, as it is evident from the figure, the two quantities do not show a good correlation: we argue that this is probably due to the fact that what mainly matters in shaping the Einstein radius is the halo triaxiality, the concentration and the presence of substructures; but we are observing in the plane of the sky a random orientation of the cluster. The second attempt has been done by correlating the weak lensing mass of the clusters with the Einstein radii. Using a Navarro-Frank-White (NFW, (Navarro et al. 1996, 1997)) model for the matter density profile, it is possible to compute the associated shear profile  $\gamma_{NFW}$  once the lens and the source redshifts have been fixed. For each simulated convergence map we compute the spherical average shear profile and measure the associated weak lensing mass  $M_{wl}$  and concentration  $c_{wl}$  by minimising

$$\chi^2(M_{wl}, c_{wl}) = \frac{\sum_i [\gamma(r_i) - \gamma_{NFW}(M_{wl}, c_{wl})]^2}{\sigma_{g,i}^2}; \quad (15)$$

$\sigma_{g,i}$  represents the shape measurement error computed assuming a number density of sources of  $20/\text{arcmin}^2$  – mimicking the number of background sources expected to be usable for weak lensing measurements in future space-based observations:

$$\sigma_{g,i} = \frac{\sigma_\epsilon}{\sqrt{n_g A_i}} \quad (16)$$

being  $A_i$  the area of the  $i$ -annulus. This method gives typically a good determination of the projected mass responsible for the lensing signal (Hoekstra et al. 2012; Giocoli et al. 2014; von der Linden et al. 2014). To summarise for each

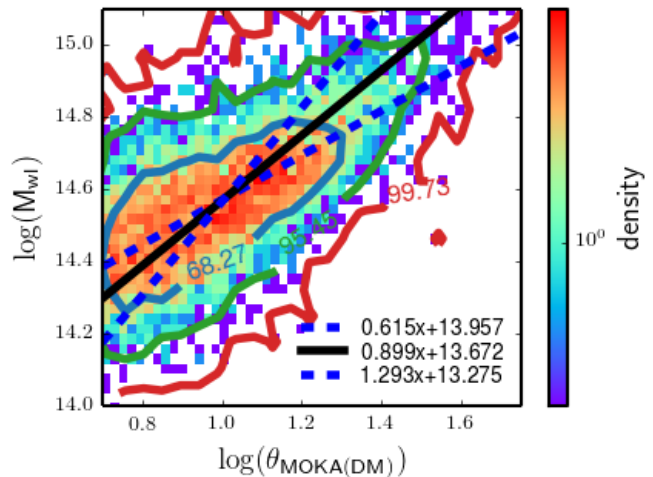


**Figure 12.** Scaling relation between the weak lensing estimated mass  $M_{wl}$  – computing the best fit profile with a NFW functional to the weak lensing shear profile – and the size of the Einstein radius. In the figure we show the relation for the DM-only run; results of the other runs are summarised in Table 3. The blue dashed lines show the best least-squares fit to the data points in the  $\log(M_{wl}) - \log(\theta_E)$  and in the  $\log(\theta_E) - \log(M_{wl})$  spaces, while the black line represents the bisector of them. The blue, green and red contours enclose 68.27, 95.45 and 99.73% of the data points, respectively.

cluster – and for each of the corresponding run (DM, Hernquist and Jaffe) – we have measured of the associated weak lensing mass and concentration in addition to the evaluation of the size of the Einstein radius. In Figure 12 we present the scaling relation – in logarithmic space and for the DM-only run – between the weak lensing cluster mass  $M_{wl}$  and the corresponding size of the Einstein radius. The blue dashed lines show the least-squares fits in the  $\log(M_{wl}) - \log(\theta_E)$  and in the  $\log(\theta_E) - \log(M_{wl})$  spaces, while the black line indicates the corresponding bisector of them. The blue, green and red curves enclose 68.27, 95.45 and 99.73% of the data points, respectively. The third relation – which offers a very strict correspondence – we have considered is between the size of the Einstein radius associated with a NFW-halo having  $M_{wl}$  and  $c_{wl}$  and the one we measure from our maps. For a NFW halo we compute  $\theta_E(M, c)$  – given its mass and concentration in addition to the lens and source redshifts – from the profile of  $[1 - \kappa(\theta) - \gamma(\theta)]$  and measuring the angular scale where the relation  $1 - \kappa(\theta_E) - \gamma(\theta_E) = 0$  holds. In Figure 13 we display this correlation – again in  $\log_{10}$  space for the DM-only run: the results for the runs with BCGs are reported in Table 3. As in the previous figure, the coloured contours enclose 68.27, 95.45 and 99.73% of the data points, the dashed blue lines displays least-squares fit in the  $\log(\theta_E(M_{wl}, c_{wl})) - \log(\theta_E)$  and in the  $\log(\theta_E) - \log(\theta_E(M_{wl}, c_{wl}))$  spaces, while the black line their bisector. In this case we notice that the correlation between the two quantities is very close, apart for some asymmetries – some systems possess an Einstein radius larger than the one computed from  $M_{wl}$  and  $c_{wl}$ . A case by case analysis of these systems has brought to two main causes: (i) large value of the ellipticity in the plane of the sky and (ii) projection of substructures close to the centre of the cluster. Both these give at the end a poor NFW fit to the shear profile,

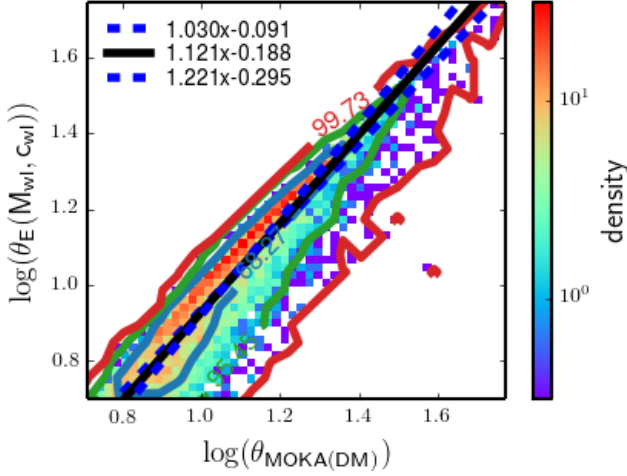


**Figure 13.** Scaling relation between the Einstein radius of a NFW halo with the same mass and concentration – computed by fitting with a NFW functional the weak lensing shear profile – and the size of the Einstein radius of the cluster. As in Fig. 12 we show the correlation only for the DM run and present in Table 3 the results for the runs with BCGs. Dashed blue lines show the least-squares fit to the data in the  $\log(\theta_E(M_{wl}, c_{wl})) - \log(\theta_E)$  and in the  $\log(\theta_E) - \log(\theta_E(M_{wl}, c_{wl}))$  spaces, while the black line displays the bisector of them.

**Table 3.** Best fit linear coefficients –  $y = mx + q$  – of all the runs (DM, Hernquist and Jaffe) of the relation displayed in Fig. 12 and 13. The superscript and subscript numbers present the coefficient of the least squares in the  $x-y$  and  $y-x$  planes, respectively.

run	$m$	$q$
$\log(M_{wl}) - \log(\theta_E)$		
DM	$0.899^{0.615}_{1.293}$	$13.672^{13.957}_{13.275}$
Hernquist	$0.892^{0.652}_{1.206}$	$13.641^{13.884}_{13.322}$
Jaffe	$0.894^{0.694}_{1.143}$	$13.589^{13.791}_{13.336}$
$\log(\theta_E(M_{wl}, c_{wl})) - \log(\theta_E)$		
DM	$1.121^{1.030}_{1.221}$	$-0.188^{-0.091}_{-0.295}$
Hernquist	$1.153^{1.066}_{1.249}$	$-0.226^{-0.132}_{-0.330}$
Jaffe	$1.168^{1.089}_{1.254}$	$-0.238^{-0.153}_{-0.331}$

leading to an underestimation of the corresponding Einstein radius associated to the NFW profile. We found that the first cause is the most probable in the majority of the cases.

#### 4 SENSITIVITY OF THE EINSTEIN RADIUS DISTRIBUTION ON $\Omega_M$ AND $\sigma_8$

The number density and the properties of galaxy clusters has been investigated by different authors with the aim of understanding how sensible they are to cosmological parameters (Rozo et al. 2010; Waizmann et al. 2012, 2014; Boldrin et al. 2016; Sartoris et al. 2015). In this section we discuss how the Einstein radius distributions are sensitive to the to-

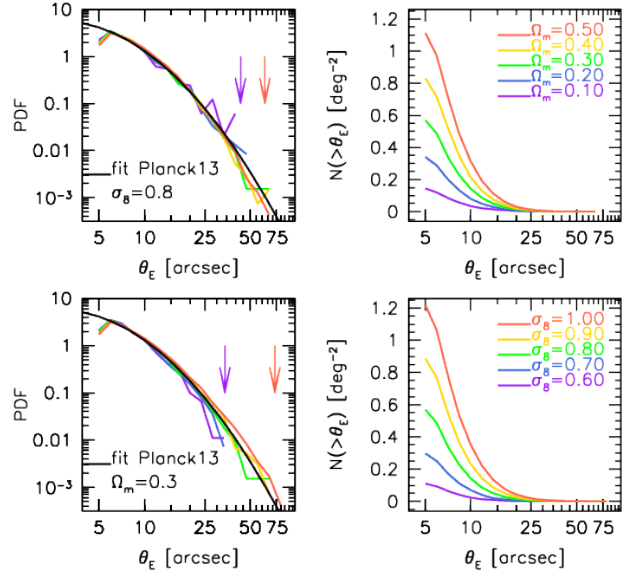


**Figure 14.** Left panels: probability distribution functions of the Einstein radius distributions of a Monte Carlo realisation of lenses at redshift  $z_l = 0.5$  with sources located at  $z_s = 2.5$  – the cluster number density has been computed from the Sheth & Tormen (1999) mass function integrated on the whole sky between  $z = 0.48$  and  $z = 0.52$ . Right panels: cumulative number counts of strong lenses per square degrees with an Einstein radius larger than a fixed value. Top and bottom panels display the case of varying  $\Omega_M$  and  $\sigma_8$  at a time, respectively. The black curve in the left panels represents the log-normal relation (eq. 17) that better describes the Planck13 probability distribution function. The arrows on the left panels mark the largest Einstein radius find in the two extreme corresponding models.

tal matter density in the Universe  $\Omega_M$  – assuming always to live in a flat universe:  $\Omega_M + \Omega_\Lambda = 1$  – and to the linear mass density r.m.s. on a scale of 8 Mpc/h  $\sigma_8$  – that defines the initial matter power spectrum normalisation. We always consider lenses located at  $z_l = 0.5$  and to obtain their abundance we randomly sample the Sheth & Tormen (1999) mass function between  $z = 0.48$  and  $z = 0.52$ . In Figure 14 we show the Probability Distribution Function (left panels) and cumulative number density per square degrees (right panels) of the Einstein radii in cosmological model with different  $\Omega_M$  (top panels) and  $\sigma_8$  (bottom panels) parameters – fixing one at a time. The vertical arrows – coloured according to the corresponding cosmological model – indicate the largest Einstein radius found in the two extreme samples assuming a full sky realisation. From the figure we notice that the Einstein radii regularly increase with  $\Omega_M$  and  $\sigma_8$ ; this is because galaxy clusters are more numerous in these cosmologies but also because they are also more concentrated; in addition we remind that clusters at  $z_l = 0.5$  in universes with higher matter content possess also a lower lensing distance  $D_{lens}$ . We underline that the BCG treatment is absent in these simulations and remind the reader that the counts can be adapted to the two considered BCG stellar density profiles at the light of the results discussed in Figures 9 and 10. In the left panels the black solid curves display the log-normal best relation to the Planck13 counts that can be read as:

$$\text{PDF}(\theta_E) = \frac{1}{\sqrt{2\pi\sigma^2}} \exp\left[-\frac{(\ln(\theta_E) - \mu)^2}{2\sigma^2}\right], \quad (17)$$

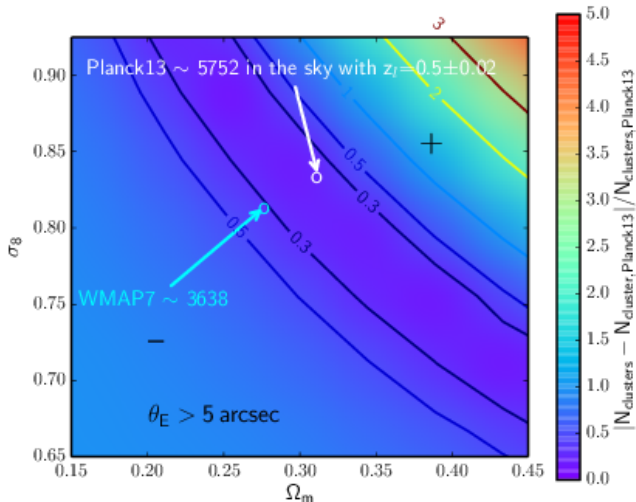


**Figure 15.** Relative counts of clusters with Einstein radius larger than 5 arcsec, with respect to the Planck13 counts, in the  $\Omega_M - \sigma_8$  plane. The black and the blue circles indicate the counts on the full sky for a Planck13 and WMAP7 cosmology, respectively. We consider the number density of cluster lenses between  $z = 0.48$  and  $z = 0.52$ , with sources at  $z_s = 2.5$ . A plus and minus signs in the plane indicate the regions where counts are positive and negative with respect to the Planck13 cosmology, respectively.

with  $\mu = 1.016$  and  $\sigma = 0.754$ . From the right panels of the figure we notice that a change of  $\Omega_M$  – or  $\sigma_8$  – of 10% corresponds approximately to a variation in the number of lenses with  $\theta_E > 5$  arcsec of about 20%.

In Figure 15 we display the relative counts of clusters with  $\theta_E$  larger than 5 arcsec, with respect to the number computed for a Planck13 cosmology, in the  $\Omega_M - \sigma_8$  plane. As reference the black and the blue circles indicate the predicted numbers of these strong lensing clusters in the whole sky between  $z_l = 0.48$  and  $z_l = 0.52$  for the Planck13 (black circle) and WMAP7 (blue cross) cosmologies. For the WMAP7 model we assume  $\Omega_M = 0.272$ ,  $\Omega_\Lambda = 0.728$ ,  $h = 0.704$  and  $\sigma_8 = 0.809$ . These results show that the expected counts of the Einstein radii in these two models may differ by more than  $3\sigma$  assuming a Poisson distribution: 5752 for the Planck13 and 3638 for the WMAP7 cosmology, respectively. We remind the reader that in computing the cluster counts for the various cosmological models we have accounted for the change of volume between  $z = 0.48$  and  $z = 0.52$ . In particular the WMAP7 model has a volume (in  $(\text{Mpc}/h)^3$ ) of about 5% larger than the Planck13 one because of a higher Hubble constant and lower total matter content, but fewer strong lensing cluster counts. This highlights that the change of volume is quite negligible with respect to the role played by the initial power spectrum normalisation parameter  $\sigma_8$  and by the different total matter content  $\Omega_M$  for the SLC counts: in Planck13 we find more clusters and those are more concentrated than in the WMAP7 cosmology because formed at higher redshifts. As already noticed by Boldrin et al. (2016) the degeneracy relation of the SLC counts behaves as the cluster counts plus the evolution of the halo structural properties in different cosmological models and the variation of the lensing distance.

## 5 SUMMARY AND CONCLUSIONS

In this paper we have presented the strong lensing properties of a sample of galaxy clusters extracted from the Millennium-XXL simulation analysing the distribution of their Einstein radius. The results have been compared with a Monte Carlo MOKA realisation of the same mass sample finding very good agreement. We have also performed an analysis to understand how sensitive is the Einstein radius distribution on specific cosmological parameters creating a sample of clusters in different models using the MOKA code. We find that the Einstein radius distribution is quite sensitive to  $\Omega_M$  and  $\sigma_8$ , as it is the cluster abundance, and that universes with high values of  $\Omega_M$  and  $\sigma_8$  possess a large number of strong lensing clusters.

In the following points we summarise the main results of our analyses:

- a large fraction of strong lensing clusters are systematically biased by projection effects;
- the orientation matters: when the major axis of the cluster ellipsoid is oriented along the line-of-sight the Einstein radius may be boosted by more than a factor of two with respect to a random orientation;
- the shape of the strong lensing population is slightly more triaxial than the overall considered cluster sample;
- a self-consistent treatment of the effects of large scale structures is important for strong lensing predictions: correlated systems may boost the Einstein radius of galaxy clusters by even more than 30%;
- the comparison between M-XXL clusters and MOKA realisations on the same sample of cluster masses shows consistent results for the Einstein radius distribution, and is well described by a log-normal distribution;
- a correct treatment of the subhalo population and the cluster triaxiality is important for an adequate strong lensing modelling: typically the triaxiality matters more and may boost the size of the cluster Einstein radii by various orders of magnitudes;
- the presence of a Bright Central Galaxy in a cluster tends to modify the total projected mass profile and consistently the size of the Einstein radius; we have discussed and modelled the impact of two different stellar mass density profiles (Hernquist 1990; Jaffe 1983) on the strong lensing properties and noticed that the Einstein radii may change by 10-60% – depending on the cluster properties and stellar profiles;
- the size of the Einstein radius has a quite tight correlation with the Einstein radius of a NFW halo where mass and concentration are computed performing a fit to the weak lensing shear profile; less stringent is the correlation with the weak lensing mass;
- the Einstein radius distribution is very sensitive to the matter content of the Universe ( $\Omega_M$ ) and to the initial power spectrum normalisation ( $\sigma_8$ ): we have noticed that universes with larger values of those parameters possess a higher number of strong lensing clusters; this can help distinguish Planck13 and WMAP7 cosmology at  $3\sigma$ .

In conclusion, our results encourage in shading more light into the dark components of our Universe through the study of strong lensing cluster populations, foreseeing

the unique results that will be available from the next-generation wide field surveys from space.

## ACKNOWLEDGMENTS

CG thanks CNES for financial support. ML acknowledges the Centre National de la Recherche Scientifique (CNRS) for its support. This work was performed using facilities offered by CeSAM (Centre de donneS Astrophysique de Marseille (<http://lam.oamp.fr/cesam/>)). This work was granted access to the HPC resources of Aix-Marseille Universite financed by the project Equip@Meso (ANR-10-EQPX-29-01) of the program "Investissements d'Avenir" supervised by the Agence Nationale pour la Recherche (ANR). This work was carried out with support of the OCEVU Labex (ANR-11-LABX-0060) and the A\*MIDEX project (ANR-11-IDEX-0001-02) funded by the "Investissements d'Avenir" French government program managed by the ANR. We acknowledge support from the Programme National de Cosmologie et Galaxie (PNCG). MM acknowledges support from Ministry of Foreign Affairs and International Cooperation, Directorate General for Country Promotion, from INAF via PRIN-INAF 2014 1.05.01.94.02, and from ASI via contract ASI/INAF/I/023/12/0. LM acknowledges the grants ASI n.I/023/12/0 "Attività relative alla fase B2/C per la missione Euclid", MIUR PRIN 2010-2011 "The dark Universe and the cosmic evolution of baryons: from current surveys to Euclid" and PRIN INAF 2012 "The Universe in the box: multiscale simulations of cosmic structure". REA acknowledges support from AYA2015-66211-C2-2. EJ acknowledge CNES support. CG thanks Mauro Sereno, Jesus Vega and Michele Boldrin for useful discussions and python stratagems. We also thank Giuseppe Tormen and Vincenzo Mezzalira for giving us the possibility to use their computer facilities on which part of the MOKA simulations have been run.

This paper has been typeset from a  $\text{\LaTeX}$  file prepared by the author.

## References

- Angulo R. E., Chen R., Hilbert S., Abel T., 2014, MNRAS, 444, 2925
- Angulo R. E., Springel V., White S. D. M., Jenkins a., Baugh C. M., Frenk C. S., 2012, MNRAS, 426, 2046
- Atek H., Richard J., Kneib J.-P., Clement B., Egami E., Ebeling H., Jauzac M., Jullo E., Laporte N., Limousin M., Natarajan P., 2014, ApJ, 786, 60
- Bacon D. J., Amara A., Read J. I., 2010, MNRAS, 409, 389
- Bartelmann M., 2010, Classical and Quantum Gravity, 27, 233001
- Bartelmann M., Schneider P., 2001, Physics Reports, 340, 291
- Bellagamba F., Maturi M., Hamana T., Meneghetti M., Miyazaki S., Moscardini L., 2011, MNRAS, 413, 1145
- Blumenthal G. R., Faber S. M., Flores R., Primack J. R., 1986, ApJ, 301, 27
- Boldrin M., Giocoli C., Meneghetti M., Moscardini L., 2012, MNRAS, 427, 3134
- Boldrin M., Giocoli C., Meneghetti M., Moscardini L., Tormen G., Biviano A., 2016, MNRAS, 457, 2738
- Bonamigo M., Despali G., Limousin M., Angulo R., Giocoli C., Soucail G., 2015, MNRAS, 449, 3171
- Borgani S., Kravtsov A., 2011, Advanced Science Letters, 4, 204
- Boylan-Kolchin M., Springel V., White S. D. M., Jenkins A., Lemson G., 2009, MNRAS, 398, 1150
- Bradač M., Clowe D., Gonzalez A. H., Marshall P., Forman W., Jones C., Markevitch M., Randall S., Schrabback T., Zaritsky D., 2006, ApJ, 652, 937
- Broadhurst T., Huang X., Frye B., Ellis R., 2000, ApJ, 534, L15
- Bryan G. L., Norman M. L., 1998, ApJ, 495, 80
- Choi J.-H., Weinberg M. D., Katz N., 2007, MNRAS, 381, 987
- Codis S., Pichon C., Pogosyan D., 2015, MNRAS, 452, 3369
- Coe D., Zitrin A., Carrasco M., Shu X., Zheng W., Postman M., Bradley L., Koekemoer et al. 2013, ApJ, 762, 32
- Cooray A., Sheth R., 2002, Physics Reports, 372, 1
- De Lucia G., Kauffmann G., Springel V., White S. D. M., Lanzoni B., Stoehr F., Tormen G., Yoshida N., 2004, MNRAS, 348, 333
- Despali G., Giocoli C., Angulo R. E., Tormen G., Sheth R. K., Baso G., Moscardini L., 2015, ArXiv e-prints
- Despali G., Giocoli C., Tormen G., 2014, MNRAS, 443, 3208
- Donahue M., Ettori S., Rasia E., Sayers J., Zitrin A., Meneghetti M., Voit G. M., Golwala S., Czakon N., Yepes G., Baldi A., Koekemoer A., Postman M., 2016, ApJ, 819, 36
- Donnarumma A., Ettori S., Meneghetti M., Gavazzi R., Fort B., Moscardini L., Romano A., Fu L., Giordano F., Radovich M., Maoli R., Scaramella R., Richard J., 2011, A&A, 528, A73
- Einstein A., 1918, Sitzungsberichte der Königlich Preussischen Akademie der Wissenschaften (Berlin), Seite 448-459.
- Eke V. R., Cole S., Frenk C. S., 1996, MNRAS, 282, 263
- Formicola I., Radovich M., Meneghetti M., Mazzotta P., Grado A., Giocoli C., 2016, MNRAS
- Gao L., White S. D. M., Jenkins A., Stoehr F., Springel V., 2004, MNRAS, 355, 819
- Giocoli C., Jullo E., Metcalf R. B., de la Torre S., Yepes G., Prada F., Comparat J., Goettlober S., Kyplin A., Kneib J.-P., Petkova M., Shan H., Tessore N., 2015, ArXiv e-prints
- Giocoli C., Meneghetti M., Bartelmann M., Moscardini L., Boldrin M., 2012a, MNRAS, 421, 3343
- Giocoli C., Meneghetti M., Metcalf R. B., Ettori S., Moscardini L., 2014, MNRAS, 440, 1899
- Giocoli C., Tormen G., Sheth R. K., 2012b, MNRAS, 422, 185
- Giocoli C., Tormen G., Sheth R. K., van den Bosch F. C., 2010a, MNRAS, 404, 502
- Giocoli C., Tormen G., van den Bosch F. C., 2008, MNRAS, 386, 2135
- Gnedin O. Y., Ceverino D., Gnedin N. Y., Klypin A. A., Kravtsov A. V., Levine R., Nagai D., Yepes G., 2011, ArXiv e-prints

- Guzzo L., Scodeggio M., Garilli B., Granett B. R., Fritz A., Abbas U., Adami C., Arnouts et al. 2014, *A&A*, 566, A108
- Hayashi E., Navarro J. F., Taylor J. E., Stadel J., Quinn T., 2003, *ApJ*, 584, 541
- Hennawi J. F., Dalal N., Bode P., Ostriker J. P., 2007, *ApJ*, 654, 714
- Hernquist L., 1990, *ApJ*, 356, 359
- Hilbert S., White S. D. M., Hartlap J., Schneider P., 2008, *MNRAS*, 386, 1845
- Hoekstra H., Bartelmann M., Dahle H., Israel H., Limousin M., Meneghetti M., 2013, *Space Sci.Rev.*, 177, 75
- Hoekstra H., Mahdavi A., Babul A., Bildfell C., 2012, *MNRAS*, 427, 1298
- Jaffe W., 1983, *MNRAS*, 202, 995
- Jing Y. P., Suto Y., 2002, *ApJ*, 574, 538
- Jullo E., Kneib J.-P., Limousin M., Elíasdóttir Á., Marshall P. J., Verdugo T., 2007, *New Journal of Physics*, 9, 447
- Jullo E., Natarajan P., Kneib J.-P., D'Aloisio A., Limousin M., Richard J., Schimd C., 2010, *Science*, 329, 924
- Katayama H., Hayashida K., Takahara F., Fujita Y., 2003, *ApJ*, 585, 687
- Keeton C. R., 2001, *ApJ*, 561, 46
- Keeton C. R., 2003, *ApJ*, 584, 664
- Koopmans L. V. E., Bolton A., Treu T., Czoske O., Auger M. W., Barnabè M., Vegetti S., Gavazzi R., Moustakas L. A., Burles S., 2009, *ApJ*, 703, L51
- Koopmans L. V. E., Treu T., Bolton A. S., Burles S., Moustakas L. A., 2006, *ApJ*, 649, 599
- Landau L. D., Lifshitz E. M., 1971, *The classical theory of fields*
- Laureijs R., Amiaux J., Arduini S., Auguères J. ., Brinchmann J., Cole R., Cropper M., Dabin C., Duvet L., et al. 2011, *arXiv:1110.3193*
- Le Fèvre O., Tasca L. A. M., Cassata P., Garilli B., Le Brun V., Maccagni D., Pentericci L., Thomas et al. 2015, *A&A*, 576, A79
- Limousin M., Richard J., Jullo E., Jauzac M., Ebeling H., Bonamigo M., Alavi A., Clement B., Giocoli C., Kneib J. P., Verdugo T., Natarajan P., Siana B., 2015, *ArXiv e-prints*
- Lynds R., Petrosian V., 1986, in *Bulletin of the American Astronomical Society Vol. 18 of BAAS, Giant Luminous Arcs in Galaxy Clusters*. p. 1014
- Macciò A. V., Dutton A. A., van den Bosch F. C., 2008, *MNRAS*, 391, 1940
- Meneghetti M., Bartelmann M., Moscardini L., 2003, *MNRAS*, 346, 67
- Meneghetti M., Fedeli C., Pace F., Gottlöber S., Yepes G., 2010a, *A&A*, 519, A90
- Meneghetti M., Fedeli C., Zitrin A., Bartelmann M., Broadhurst T., Gottlöber S., Moscardini L., Yepes G., 2011, *A&A*, 530, A17
- Meneghetti M., Melchior P., Grazian A., De Lucia G., Dolag K., Bartelmann M., Heymans C., Moscardini L., Radovich M., 2008, *A&A*, 482, 403
- Meneghetti M., Rasia E., Merten J., Bellagamba F., Ettori S., Mazzotta P., Dolag K., Marri S., 2010b, *A&A*, 514, A93+
- Merritt D., 1985, *ApJ*, 289, 18
- Merten J., 2014, *ArXiv e-prints*
- Merten J., Meneghetti M., Postman M., Umetsu K., Zitrin A., Medezinski E., Nonino M., Koekemoer A., Melchior P., Gruen D., et al. 2015, *ApJ*, 806, 4
- Metcalf R. B., Madau P., 2001, *MNRAS*, 563, 9
- More A., Cabanac R., More S., Alard C., Limousin M., Kneib J.-P., Gavazzi R., Motta V., 2012, *ApJ*, 749, 38
- Navarro J. F., Frenk C. S., White S. D. M., 1996, *ApJ*, 462, 563
- Navarro J. F., Frenk C. S., White S. D. M., 1997, *ApJ*, 490, 493
- Newman A. B., Treu T., Ellis R. S., Sand D. J., 2011, *ApJ*, 728, L39+
- Oguri M., Blandford R. D., 2009, *MNRAS*, 392, 930
- Oguri M., Takada M., Umetsu K., Broadhurst T., 2005, *ApJ*, 632, 841
- Paczynski B., 1987, *Nature*, 325, 572
- Percival W. J., Ross A. J., Sánchez A. G., Samushia L., Burden A., Crittenden R., Cuesta A. J., et al. 2014, *MNRAS*, 439, 2531
- Petkova M., Metcalf R. B., Giocoli C., 2014, *MNRAS*, 445, 1954
- Planck Collaboration Ade P. A. R., Aghanim N., Alves M. I. R., Armitage-Caplan C., Arnaud M., Ashdown M., Atrio-Barandela F., Aumont J., Aussel H., et al. 2014, *A&A*, 571, A1
- Postman M., Coe D., Benítez N., Bradley L., Broadhurst T., Donahue M., Ford H., Graur et al. 2012, *ApJS*, 199, 25
- Puchwein E., Hilbert S., 2009, *MNRAS*, 398, 1298
- Radovich M., Formicola I., Meneghetti M., Bartalucci I., Bourdin H., Mazzotta P., Moscardini L., Ettori S., Arnaud M., Pratt G. W., Aghanim N., Dahle H., Douspis M., Pointecouteau E., Grado A., 2015, *A&A*, 579, A7
- Rau S., Vegetti S., White S. D. M., 2013, *MNRAS*, 430, 2232
- Redlich M., Bartelmann M., Waizmann J.-C., Fedeli C., 2012, *A&A*, 547, A66
- Richard J., Pelló R., Schaerer D., Le Borgne J.-F., Kneib J.-P., 2006, *A&A*, 456, 861
- Rozo E., Wechsler R. H., Rykoff E. S., Annis J. T., Becker M. R., Evrard A. E., Frieman J. A., Hansen et al. 2010, *ApJ*, 708, 645
- Saha P., Williams L. L. R., 2006, *ApJ*, 653, 936
- Sand D. J., Treu T., Ellis R. S., 2002, *ApJ*, 574, L129
- Sanderson A. J. R., Edge A. C., Smith G. P., 2009, *MNRAS*, 398, 1698
- Sartoris B., Biviano A., Fedeli C., Bartlett J. G., Borgani S., Costanzi M., Giocoli C., Moscardini L., Weller J., Ascaso B., Bardelli S., Maurogordato S., Viana P. T. P., 2015, *arXiv:1505.02165*
- Serjeant S., 2014, *ApJ*, 793, L10
- Sharon K., Gladders M. D., Rigby J. R., Wuyts E., Bayliss M. B., Johnson T. L., Florian M. K., Dahle H., 2014, *ApJ*, 795, 50
- Shaw L. D., Weller J., Ostriker J. P., Bode P., 2006, *ApJ*, 646, 815
- Sheth R. K., Tormen G., 1999, *MNRAS*, 308, 119
- Soucail G., Fort B., Mellier Y., Picat J. P., 1987, *A&A*, 172, L14
- Soucail G., Kneib J.-P., Golse G., 2004, *A&A*, 417, L33
- Soucail G., Mellier Y., Fort B., Cailloux M., 1988b, *A&AS*, 73, 471
- Soucail G., Mellier Y., Fort B., Mathez G., Cailloux M.,

- 1988a, *A&A*, 191, L19
- Sousbie T., Pichon C., Colombi S., Novikov D., Pogosyan D., 2008, *MNRAS*, 383, 1655
- Sousbie T., Pichon C., Kawahara H., 2011, *MNRAS*, 414, 384
- Springel V., White S. D. M., Jenkins A., Frenk C. S., Yoshida N., Gao L., Navarro J., Thacker R., Croton D., Helly J., Peacock J. A., Cole S., Thomas P., Couchman H., Evrard A., Colberg J., Pearce F., 2005, *Nature*, 435, 629
- Springel V., White S. D. M., Tormen G., Kauffmann G., 2001b, *MNRAS*, 328, 726
- The Dark Energy Survey Collaboration 2005, *ArXiv Astrophysics e-prints*
- Tormen G., 1998, *MNRAS*, 297, 648
- Tormen G., Moscardini L., Yoshida N., 2004, *MNRAS*, 350, 1397
- Vale C., White M., 2003, *ApJ*, 592, 699
- van den Bosch F. C., Tormen G., Giocoli C., 2005, *MNRAS*, 359, 1029
- Verdugo T., Motta V., Muñoz R. P., Limousin M., Cabanac R., Richard J., 2011, *A&A*, 527, A124
- von der Linden A., Allen M. T., Applegate D. E., Kelly P. L., Allen S. W., Ebeling H., Burchat P. R., Burke D. L., Donovan D., Morris R. G., Blandford R., Erben T., Mantz A., 2014, *MNRAS*, 439, 2
- Waizmann J.-C., Redlich M., Bartelmann M., 2012, *A&A*, 547, A67
- Waizmann J.-C., Redlich M., Meneghetti M., Bartelmann M., 2014, *A&A*, 565, A28
- Wang L., Li C., Kauffmann G., De Lucia G., 2006, *MNRAS*, 371, 537
- Wu X.-P., Fang L.-Z., Xu W., 1998, *A&A*, 338, 813
- Xu B., Postman M., Meneghetti M., Seitz S., Zitrin A., Merten J., Maoz D., Frye B., Umetsu K., Zheng W., Bradley L., Vega J., Koekemoer A., 2015, *ArXiv e-prints*
- Zhang Y., Miller C., McKay T., Rooney P., Evrard A. E., Romer A. K., Perfecto R., Song J., et al. 2016, *ApJ*, 816, 98
- Zhao D. H., Jing Y. P., Mo H. J., Bnörner G., 2009, *ApJ*, 707, 354
- Zitrin A., Broadhurst T., 2009b, *ApJ*, 703, L132
- Zitrin A., Broadhurst T., Barkana R., Rephaeli Y., Benítez N., 2011, *MNRAS*, 410, 1939
- Zitrin A., Broadhurst T., Bartelmann M., Rephaeli Y., Oguri M., Benítez N., Hao J., Umetsu K., 2011c, *ArXiv e-prints*
- Zitrin A., Broadhurst T., Umetsu K., Coe D., Benítez N., Ascaso B., Bradley L., Ford H., Jee J., Medezinski E., Rephaeli Y., Zheng W., 2009a, *MNRAS*, 396, 1985
- Zitrin A., Zheng W., Broadhurst T., Moustakas J., Lam D., Shu X., Huang X., Diego J. M., Ford H., Lim J., Bauer F. E., Infante L., Kelson D. D., Molino A., 2014, *ApJ*, 793, L12